A Theoretical/Numerical Study on Ultrasound Wave Coupling From Structure to Remotely Bonded Fiber Bragg Grating Ultrasound Sensor

H. Huang[1]
Department of Mechanical and Aerospace Engineering,
University of Texas at Arlington,
500 W. First Street, WH211,
Arlington, TX 76010
e-mail: huang@uta.edu

K. Balusu
Department of Mechanical and Aerospace Engineering,
University of Texas at Arlington,
500 W. First Street, WH211,
Arlington, TX 76010
e-mail: kranthi.balusu@mavs.uta.edu

Recently published experimental works on remotely bonded fiber Bragg grating (FBG) ultrasound (US) sensors show that they display some unique characteristics that are not observed with directly bonded FBG sensors. These studies suggest that the bonding of the optical fiber strongly influences how the ultrasound waves are coupled from the structure to the FBG sensor. In this paper, the analytical model of the structure-adhesive-optical fiber section, treated as an ultrasound coupler, is derived and analyzed to explain the observed experimental phenomena. The resulting dispersion curve shows that the ultrasound coupler possesses a cutoff frequency, above which a dispersive longitudinal mode exists. The low propagation speed of the dispersive longitudinal mode leads to multiple resonances at and above the cutoff frequency. To characterize the resonant characteristics of the ultrasound coupler, a semi-analytical model is implemented and the scattering parameters (S-parameters) are introduced for broadband time-frequency analysis. The simulation was able to reproduce the experiment observations reported by other researchers. Furthuremore, the behaviors of the remotely bonded FBG sensors can be explained based on its resonant characteristics. [DOI: 10.1115/1.4049372]

Keywords: structural health monitoring, optical fiber ultrasound sensor, ultrasound waveguide, scattering parameters, adhesive layer, longitudinal mode, fiber Bragg grating (FBG), elastic wave, numerical analysis, sensors, theoretical developments, ultrasonics, vibrations, wave propagation modeling

1 Introduction

Structural health monitoring (SHM) technology has been under intensive studies in the past decades because it has the potential to shift maintenance of infrastructures from safe life practice or schedule-based schemes to condition based maintenance [1–4]. Since detectable damage could take a long time to develop and its location is typically unknown, an effective SHM system should be able to detect damage over a large area without incurring significant cost or weight penalty. Due to this requirement, ultrasound (US)-based detection and optical fiber sensors are two of the most common sensing schemes for SHM systems. Ultrasound-based techniques detect the abnormalities in the ultrasound or guided waves propagating in the structures and infer the health condition of the structures from these abnormalities. Since ultrasound waves can propagate over a long distance in plates, tubes, cylinders, etc., one ultrasound transducer can cover an area that is much larger than its physical size [5,6]. Optical fiber sensors, on the other hand, detect damage based on the characteristics of light propagating inside the fiber core. They are attractive for SHM primarily due to their light weight, compact size, low cost, and immunity to electromagnetic interferences, etc. [7–9]. Among various optical fiber sensors, fiber Bragg grating (FBG) based sensors are the most widely accepted sensors [10–12]. Typically, FBG sensors are bonded directly on the structure to ensure that the FBG experiences the same displacement, and thus the strain, as the hosting structure. The displacement changes the FBG periods, leading to a shift in the FBG reflectance frequency. Compared with other optical fiber sensors, one unique advantage of the FBG sensors is that the FBG is directly inscribed into a conventional optical fiber. As such, the interface between the sensing element (i.e., the FBG section) and the optical fiber for signal transmission is seamless. Incorporating FBG sensors in an optical fiber therefore does not require labor-intensive integration. In addition, the physical measurands extracted from the spectral parameter of the FBG render the measurements more reliable, more robust, and more sensitive to minute changes. Since the reflectance spectrum of an FBG can have a very narrow bandwidth of a fraction of nanometers, multiple FBG sensors can be implemented in a single strand of optical fiber based on the principle of wavelength division multiplexing [13]. This unique feature enables deploying a large number of FBG sensors without incurring substantial cost or weight penalties.

While optical fibers are mainly used as optical waveguides, studies have been carried out in the past to investigate optical fibers as ultrasound waveguides [14–16]. Dubbed "acoustic fiber," optical fibers were considered as a means for long-distance data and energy transfer as well as delay lines [17]. A focus of these studies was on designing the mechanical properties of the fiber cladding and core to confine the ultrasound wave within the fiber core. However, analysis done by Mbamou et al. [15] concluded that "the usual glass fibers are not as good for acoustical as for optical applications." A different strategy was developed by the SHM community in exploiting the optical fiber as ultrasound waveguide sensors [18–22]. In these applications, the ultrasound wavelength of interest is much larger than the fiber diameter. As such, the optical fiber can be treated as being homogenous and the differences in the material properties of the fiber core, cladding, and coating are neglected. Based on similar principles, fibers made

[1]Corresponding author.

Manuscript received July 20, 2020; final manuscript received December 2, 2020; published online January 19, 2021. Assoc. Editor: Fabrizio Ricci.

of different materials, such as copper [23,24], aluminum [25], steel [26,27], etc., were also studied as ultrasound waveguides for environmental monitoring or epoxy curing. Compared with other SHM sensors, however, the ultrasound waveguide sensors received rather limited attention.

Recently, several researchers have implemented remotely bonded FBG ultrasound sensors, in which the optical fiber leading to the FBG is bonded on the structure, while the FBG sensor itself is at a distance away from the bonding location and is unbonded (see the Appendix for the comparison between the remotely and directly bonded FBG sensors as well as the principle of operation of FBG ultrasound sensor and its interrogation schemes) [28–35]. One advantage of such an arrangement is that when it is used for acoustic emission sensing, the remotely bonded FBG sensor can "prevent the Bragg wavelength from shifting under varying load conditions" [28]. Another advantage is that a remotely bonded FBG produce an enhanced response as compared with its directly bonded counterpart [28,29]. For example, Wee et al. reported that "the increase in sensitivity was demonstrated to be 5.1 times that of the directly bonded case" [29]. On the other hand, the adhesive condition could have a strong influence on the ultrasound waves coupled to the optical fiber and thus the response of the remotely bonded FBGs. Specifically, the FBG response was seen to increase with the adhesive length up to a certain distance [31]. In addition, both backward and forward-propagating ultrasound waves were observed when the optical fiber was bonded on the structure using adhesive [32]. In contrast, an adhesive tape produces predominately forward-propagating waves in the fiber. Another interesting observation was that the optical fiber only supports the longitudinal waves [30,35], which could be an advantage or a disadvantage. As an advantage, it provides a means to separate the longitudinal modes from the other ultrasound modes [35]. The disadvantage is that other ultrasound modes may be more sensitive to certain types of damage and could provide more information about the damage. While finite element simulations can reproduce some of the behaviors of remotely bonded FBG ultrasound sensors [36], the physics underlying such behaviors is not known at this point.

In this paper, we present an analytical model for studying ultrasound wave coupling between two ultrasound waveguides, e.g., a structure and an optical fiber, through an adhesive layer. Treating the structure-adhesive-fiber section as an ultrasound coupler having four ports, the concept of scattering parameters is introduced to characterize its resonant characteristics. The response of the ultrasound coupler to a narrowband tone-burst input is simulated numerically by varying the parameters of the adhesive layer. These parametric studies reproduce the experimental observations reported in the literature and provide physical explanation to these observations.

2 Analytical and Numerical Simulation Model

The physical model of an optical fiber bonded to a structure is shown in Fig. 1(*a*). In finite element simulation models [30,35,36], the optical fiber is fully or partially encapsulated in the top portion of the adhesive layer. Assuming the ultrasound wave originates at the left side of the structure and propagates toward the bonded section, upon encountering the bonded section, it is coupled to the optical fiber in both forward (i.e., to the right) and backward (i.e., to the left) propagating directions. The physical model is idealized as the simplified model shown in Fig. 1(*b*), in which the top portion of the adhesive with the embedded optical fiber is homogenized as a superstrate with material properties differing from the rest of the adhesive layer. The optical fibers leading to and from the bonded section are assumed to be connected to the superstrate at the edges. Since the optical fiber only supports the longitudinal wave [30], the simplified model shown in Fig. 1(*b*) can be represented by the one-dimensional (1D) extensional bar model shown in Fig. 1(*c*). Considering that the optical fiber is very light and has a very low attenuation, the forward and backward propagating ultrasound waves in the optical fibers are expected to have the same amplitudes as the displacements at the left and right edges of the superstrate, respectively. Therefore, including the optical fibers in the 1D simulation model is not necessary. Ultrasound waves are generated by applying a time-varying force at the left edge of the substrate. The response of the system to this time-varying force is calculated in the frequency domain, following a procedure described in Refs. [37,38]. Two absorption sections were added to the left and right ends of the substrate (i.e., the structure) to eliminate any reflections that may cause numerical aliasing. To minimize the refection at the absorber–substrate interface, the material properties of the absorption sections are identical to those of the substrate except that they have a very small mechanical loss coefficient and a very large length (e.g., 100 m). By implementing the model semi-analytically without dividing the absorbers into small elements, the large lengths do not introduce any additional computation burden.

The 1D simulation model is sectioned along the interfaces where the cross-sectional area changes, i.e., at the edges of the ultrasound coupler and the absorber–substrate interfaces. As such, the model can be divided into two types of homogenous section, i.e., the absorber/ substrate section and the ultrasound coupler section. For the absorber/substrate sections, the extensional bar model is adopted to simulate the longitudinal ultrasound modes. For the ultrasound coupler, its governing equation can be derived assuming the displacements of the substrate and superstrate are coupled through the shear deformation of the adhesive layer [37,38] (see Fig. 2). As such, the shear stress τ of the adhesive layer can be expressed as

$$\tau(x,t) = G_a\gamma_a = G_a\left[\frac{u_b(x,t) - u_p(x,t)}{h_a}\right] \tag{1}$$

where γ_a is the shear strain of the adhesive and G_a is the adhesive shear modulus. The subscribes b, p, a represent the substrate, the

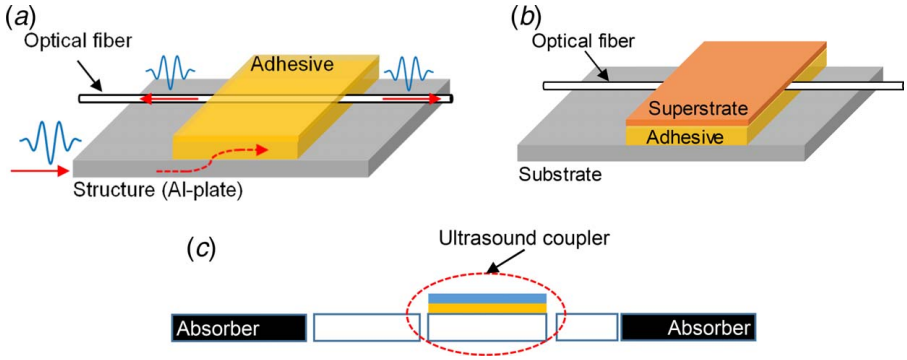

Fig. 1 Simulating longitudinal ultrasound wave coupling from the structure to the optical fiber: (*a*) physical model, (*b*) idealized model, and (c) 1D simulation model

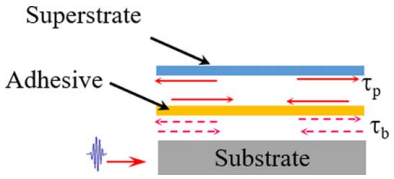

Fig. 2 Coupling the displacements of the substrate and superstrate through the shear deformation of the adhesive layer

superstrate, and the adhesive, respectively. u represents the displacement and h represents the thickness.

The governing equations for the longitudinal deformations of the substrate and superstrate are [37,39,40]

$$\frac{\partial^2 u_b}{\partial x^2} - \frac{\rho_b}{E_b}\frac{\partial^2 u_b}{\partial t^2} = -\frac{\tau_b}{E_b h_b} \tag{2a}$$

and

$$\frac{\partial^2 u_p}{\partial x^2} - \frac{\rho_p}{E_p}\frac{\partial^2 u_p}{\partial t^2} = \frac{\tau_p}{E_p h_p} \tag{2b}$$

in which, ρ and E stand for the density and the Young's modulus. $\tau_b = \tau$ and $\tau_p = \alpha\tau$ for an adhesive having a shear transfer ratio of α. Combining Eqs. (1) and (2) results in an analytical governing equation for the ultrasound coupler, i.e.

$$\frac{\partial^4 \bar{u}_p}{\partial x^4} + A\frac{\partial^2 \bar{u}_p}{\partial x^2} + B\bar{u}_p = 0 \tag{3}$$

whose solution is

$$\bar{u}_p(x) = a_i e^{\beta_i x} + d_i e^{-\beta_i x}, \quad i = 1,\ 2 \tag{4}$$

in which β_i are the roots of

$$\beta_i^4 + A\beta_i^2 + B = 0 \tag{5}$$

The two constants A and B are functions of the geometrical and mechanical properties of the substrate, superstrate, and adhesive layer as well as the angular frequency ω, i.e.

$$A = \frac{C_2}{C_1} + \frac{\rho_b}{E_b}\left(\omega^2 - \frac{\alpha}{\rho_b h_b}\frac{G_a}{h_a}\right) \tag{6a}$$

$$B = \frac{C_2}{C_1}\frac{\rho_b}{E_b}\left(\omega^2 - \frac{\alpha}{\rho_b h_b}\frac{G_a}{h_a}\right) + \frac{\alpha}{C_1}\frac{\rho_b}{E_b}\frac{1}{\rho_b h_b}\frac{G_a}{h_a} \tag{6b}$$

$$C_1 = -(\rho_p h_p)\left(\frac{E_p}{\rho_p}\right)\left(\frac{h_a}{G_a}\right) \tag{6c}$$

and

$$C_2 = 1 - \omega^2(\rho_p h_p)\left(\frac{h_a}{G_a}\right) \tag{6d}$$

The design parameters of the ultrasound coupler, therefore, include the Young's modulus-density ratio E_b/ρ_b as well as the density-thickness product $\rho_b h_b$ of the substrate and superstrate, and two adhesive parameters, i.e., the shear modulus-thickness ratio G_a/h_a and the shear transfer ratio α.

3 Propagation Modes and Dispersion Curve of Ultrasound Coupler—Analytical Solution

The resonant characteristics of the ultrasound coupler can be explained based on the governing equation given in Eq. (5). The characteristic roots of the Eq. (5) can be expressed as

$$\beta_1 = \sqrt{\frac{-A - \sqrt{A^2 - 4B}}{2}} \quad \text{and} \quad \beta_2 = \sqrt{\frac{-A + \sqrt{A^2 - 4B}}{2}} \tag{7}$$

To support wave propagation, at least one of the roots β_i, $i = 1, 2$ must be complex. Since

$$\Delta = A^2 - 4B = \left[\frac{C_2}{C_1} - \frac{1}{E_b}\left(\rho_b\omega^2 - \frac{\alpha G_a}{h_b h_a}\right)\right]^2 + 4\frac{\alpha G_a}{E_b h_b h_a} \times \frac{G_a}{E_p h_p h_a} > 0 \tag{8}$$

whether β_i is complex or not depends on the signs of A and B. As tabulated in Table 1, the ultrasound coupler supports only one mode if $B < 0$ or $B = 0 \wedge A > 0$ and it supports two modes if $B > 0 \wedge A \geq 0$. Consequently, the cutoff frequency for the second propagation mode can be analytically solved by setting $B = 0$, i.e.

$$f_c = \frac{\omega_c}{2\pi} = \frac{1}{2\pi}\sqrt{\frac{G_a}{h_a}\left(\frac{\alpha}{h_b\rho_b} + \frac{1}{h_p\rho_p}\right)} \tag{9}$$

Clearly, f_c is dependent of the adhesive property G_a/h_a as well as the substrate and superstrate mass parameters, $h_b\rho_b$, and $h_p\rho_p$. On the other hand, it is independent of the Young's moduli of the substrate or superstrate.

The dispersion curve of the ultrasound coupler, which represents the relationship between the group velocities of the two modes and the frequency, is calculated from the characteristic roots β_i and shown in Fig. 3. The substrate is an aluminum alloy with mechanical properties as the followings: Young's modulus $E = 71$ GPa, density $\rho = 2770$ kg/m^3, and Poisson's ratio $\upsilon = 0.33$. The superstrate is assumed to have the same properties as the optical fiber, i.e., $E = 66$ GPa, $\rho = 2170$ kg/m^3, and $\upsilon = 0.15$ (see tabe 1 in Wee et al. [36]). The mechanical properties of the adhesive are typically unknown, and their values provided in the publications can vary

Table 1 Relationship between the signs of *A* and *B* and the characteristic roots of ultrasound coupler's governing equation

	$A<0$		$A=0$		$A>0$	
	β_1	β_2	β_1	β_2	β_1	β_2
$B<0$	C	R	C	R	C	R
$B=0$	R	R	0	0	C	R
$B>0$	R	R	C	C	C	C

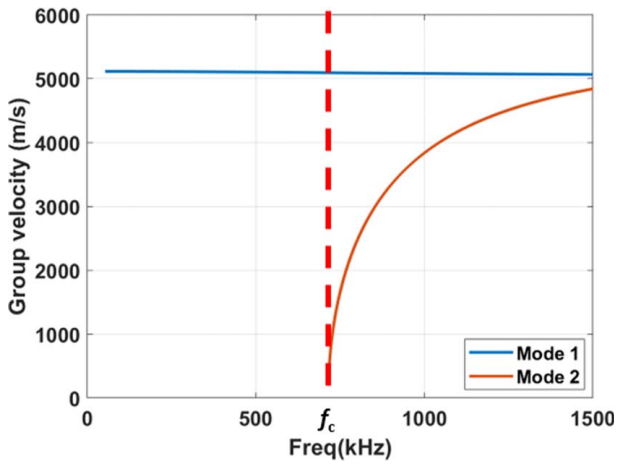

Fig. 3 Dispersion curve of an ultrasound coupler showing the ultrasound wave modes it supports below and above the cutoff frequency f_c

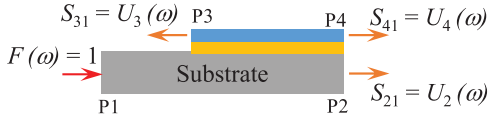

Fig. 4 Representing the ultrasound coupler as a 4-port network and S-parameters

widely [41,42]. To study the adhesive effects, it is common to vary the adhesive properties in a selected range [36,37,43]. The adhesive for this study is initially assumed to have a Young's modulus of 2.5 GPa and a Poisson ratio of $\upsilon = 0.39$. For an adhesive thickness of 185 μm, a substrate thickness of 0.8 mm, and a superstrate thickness of 125 μm, the cutoff frequency of the coupler is calculated from Eq. (9) as 713 kHz. Below the cutoff frequency, there is only one propagation mode with a group velocity identical to that of the substrate. Above the cutoff frequency, one propagation mode has a group velocity that reduces at a very gradual rate with the increasing frequencies. The group velocity of the second propagation mode, however, increases rapidly from zero at f_c and approaches that of the substrate at high frequencies. In other words, the ultrasound coupler supports a dispersive wave above the cutoff frequency. This is different from conventional extensional bars, which only have one nondispersive mode [44].

4 Resonant Characteristics of Ultrasound Coupler—S-parameter Representation

Once the governing equation for the ultrasound coupler is established, the numerical simulation of the 1D model shown in Fig. 1(*c*) can be implemented by adopting the reverberation matrix method (RMM) described in Refs. [45,46] and applying the boundary and continuity conditions [37,38]. For more detailed descriptions of the RMM and the simulation method, the readers should refer to the cited Refs. [37,38,45,46]. Since the constants A and B are functions of the angular frequency ω, it is expected that the behavior of the ultrasound coupler is frequency dependent. Therefore, a broadband analysis of the ultrasound coupler is necessary, which can be facilitated using the S-parameters [47], a concept that is commonly used in the microwave community for representing a linear-time-invariant network. As shown in Fig. 4, an ultrasound coupler can be considered as a 4-port network; port 1 and 2 represent the left and right edges of the substrate while port 3 and 4 represent the left and right edges of the superstrate, respectively. The transmission S-parameter S_{j1} is the frequency spectrum of the output $u_j(x, \omega_i)$ at port j ($j = 2$, 3, and 4), when the ultrasound is generated at port 1 using an impulse force $F(\omega_i) = 1$. Port 1 is selected to be at several wavelengths away from the left edge of the bonding section to eliminate the edge resonance effect (see discussions in Sec. 5.1). Once the S-parameters are available, the time-frequency response of the ultrasound coupler can be calculated using the procedure described in Refs. [47,48].

Figure 5 shows the S-parameters for three different adhesive lengths L_a. When L_a is small, i.e., $L_a = 1$ mm, only one resonant peak is observed at the cutoff-frequency f_c, due to the very small group velocity of the dispersive ultrasound mode. As L_a increases to 10 mm, four additional resonant peaks appear above f_c. Below f_c, the S41 curve only has a slight "bulge" at around 100 kHz, as highlighted by the circle. However, it is difficult to discern whether it is a resonant peak or not. At $L_a = 50$ mm, the number of resonance peaks increased dramatically above f_c. In addition, there are clear resonant peaks below f_c, e.g., at 83, 130, 178 kHz,

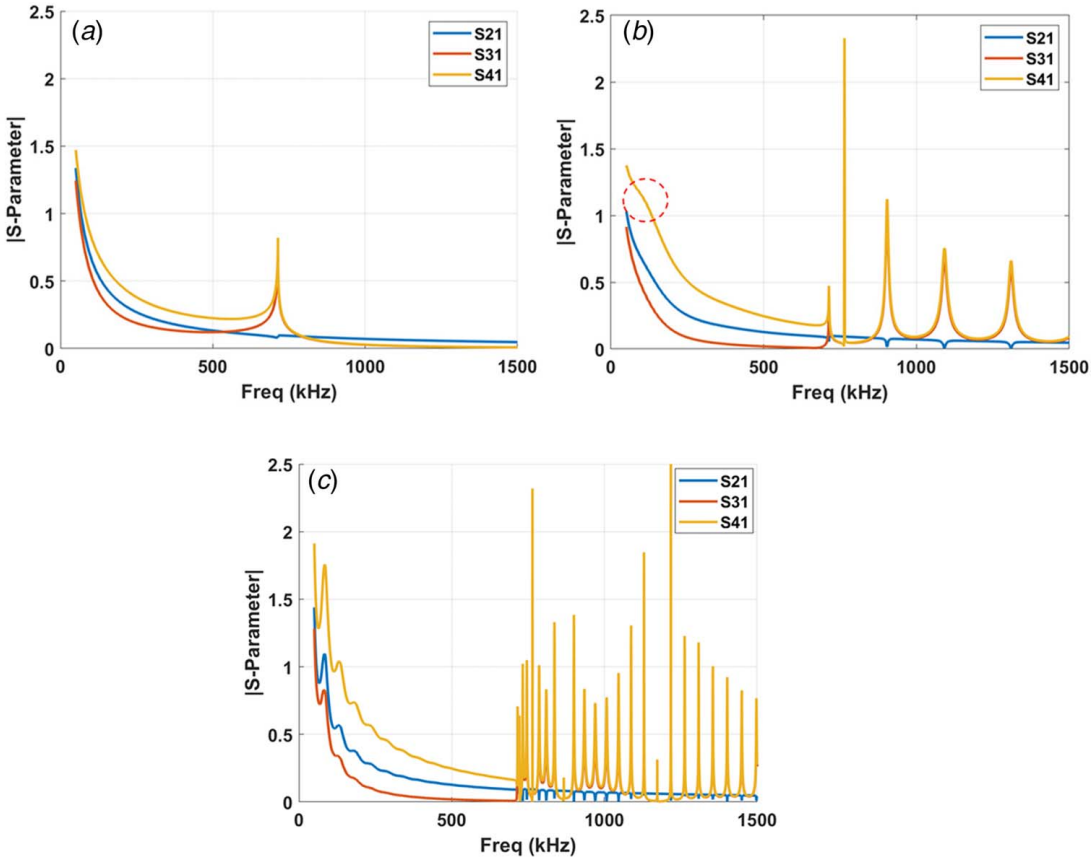

Fig. 5 Effect of adhesive length L_a on the S-parameters of the ultrasound coupler: (*a*) $L_a = 1$ mm, (*b*) $L_a = 10$ mm, and (*c*) $L_a = 50$ mm

etc. It is interesting to note that the resonant peak at f_c exists regardless of the adhesive length L_a while the other resonant peaks change locations with L_a and the number of resonant peaks increases with L_a. We suspect that the resonance peaks are related to the ultrasound waves being bounced back and forth between the two free edges of the superstrate. If this hypothesis is true, the resonance frequencies would be functions of the propagation speed and the bonding length. This explains why a resonance peak exists at the cutoff frequency f_c with any bonding length because of the low propagation speed at f_c. Verifying such a hypothesis, however, would require more extensive investigations and will be a subject of future study. The S21 curve displays a few notches at high frequencies. These notches represent the antiresonances, which is similar to the ultrasound spectrum generated using a surface bonded piezoelectric wafer active transducer [5,49]. Notice also that these notches have very narrow bandwidths. In order to observe these notches experimentally, broadband frequency-domain measurements, such as laser ultrasonics, may be needed and will be a subject of future study.

5 Explanations of Experimental Observations

Taking advantage of the computation efficiency and time-frequency analysis capability of the simulation model, we were able to perform comprehensive parametric studies on the bonding condition of remotely bonded FBG sensors. These studies provide the theoretical explanations to the experimental observations reported in published works [29,31–33], as discussed below.

5.1 Why Does Remotely Bonded Fiber Bragg Gratings Display Enhanced Sensor Responses? Wee et al. reported that the response of a remotely bonded FBG could be five times larger than if the FBG is directly bonded [29]. When an FBG is bonded directly on a structure, the adhesive typically covers the entire length of the FBG and even the optical fiber leading to and from the FBG. Therefore, the displacement measured by a directly bonded FBG can be approximated as the displacements at the center of the superstrate. In contrast, when the FBG is bonded on the structure remotely, the displacements at the edges of the superstrate is coupled to the optical fiber. The spectra of the displacements at three locations of the superstrate, i.e., at the left edge, the center, and the right edge, for an adhesive length of 10 mm, are shown in Fig. 6(*a*). Below the cutoff frequency f_c, the displacements at the right edge of the superstrate are consistently larger than the displacements at the center or at the left edge. Above f_c, however, both edges experience the same displacements while the center has a slightly lower displacement, except at the resonant peaks. The maximum displacements along the length of the substrate and superstrate are shown in Fig. 6(*b*), generated using a 300 kHz 5.5 cycle tone-burst excitation. Near the left edge of the ultrasound coupler (i.e., at $x = 0.2$ m), the maximum displacement of the substrate fluctuates along the length and the displacement at the left edge of the superstrate is substantially smaller than the rest of the superstrate. In contrast, the right edge of the superstrate displays a substantially larger maximum displacement than other locations. Away from the edges, the substrate and superstrate of the ultrasound coupler have almost identical displacements. The

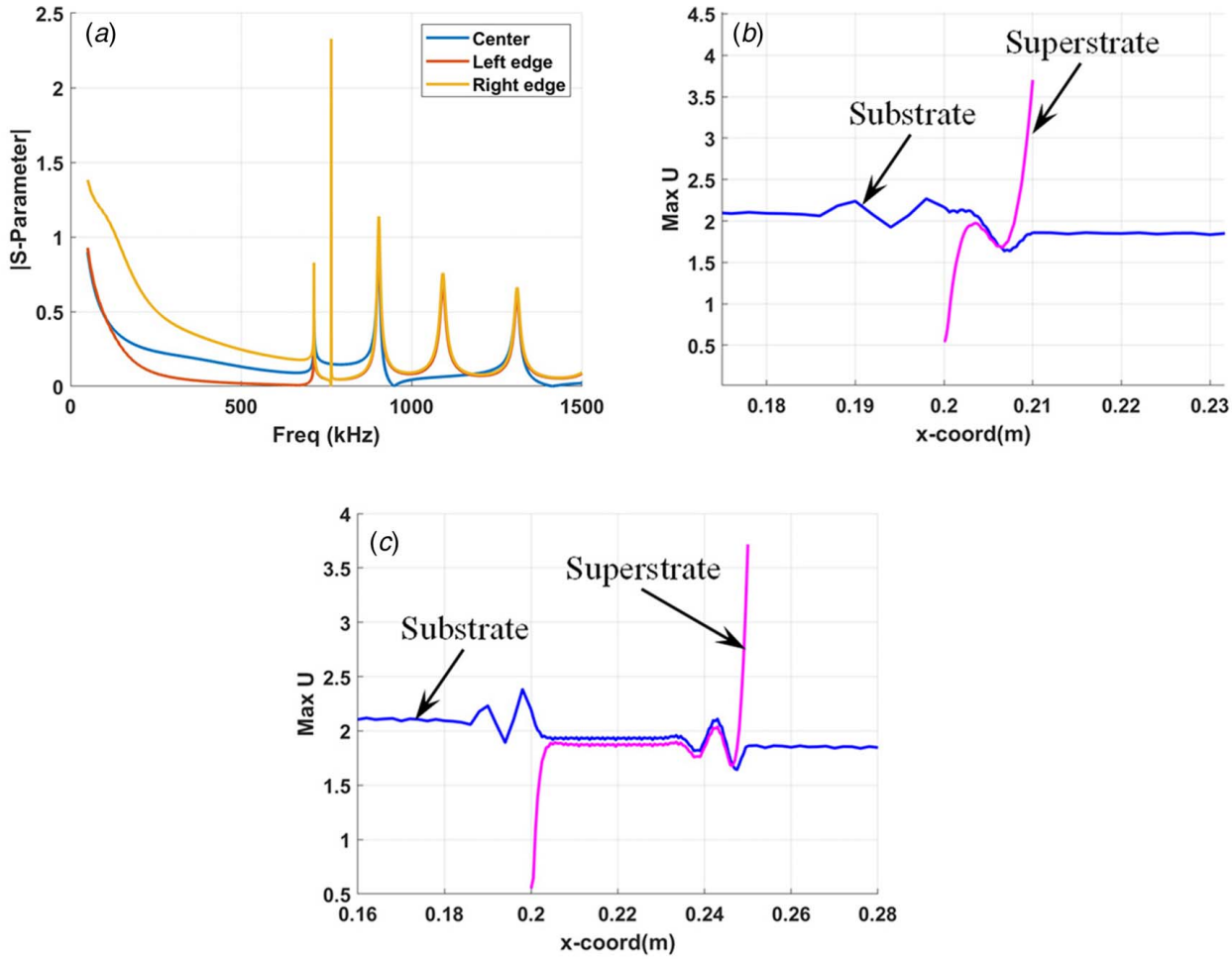

Fig. 6 Comparison of the substrate and superstrate displacements: (*a*) S-parameters at the center and two edges of the superstrate; and the maximum displacements along the length for (*b*) $L_a = 10$ mm and (c) $L_a = 50$ mm, assuming a 300 kHz 5.5 cycle tone-burst excitation

differences in the maximum displacements at the edges and at the center of the ultrasound coupler is due to the edge resonance effect. Edge resonant effect refers to the generation of large displacements in the near-field of scattering sources, such as free edges [50,51], step cross-sectional changes [52,53], cracks [54,55], wedges [56], etc. At a scattering source, waves with propagation constants different from that of the incident waves are excited in order to satisfy the boundary condition. The interference of the incident and scattered waves leads to wave enhancements in the immediate vicinity of the scattering source [54,57,58]. This effect is more obvious when the adhesive length increases to 50 mm, as shown in Fig. 6(*c*). In this case, the large displacements are seen at the locations of the substrate close to the left edge of the coupler and at the right edge of the superstrate. The displacements decay rapidly with the distance near the edges and remains constants at locations that are more than about one wavelength away from the edges. It worth noting that the substrate also displays some edge effects near the edges of the bonded section, albeit the amplitude is much smaller than the superstrate. This is because the substrate is continuous while the superstrate has two free edges. In other words, the substrate sections to the left and right side of the bonded section limit the displacement of the substrate under the superstrate.

While the present work is focused on the remotely bonded FBG ultrasound sensor, some insights can be also drawn with respect to the directly bonded FBG sensors. For the directly bonded FBG sensors, the assumption is that the displacement experienced by the FBG sensor is the same as that of the structure. This is true only when the FBG sensor is more than one or two wavelengths away from the edges of the adhesive, as Figs. 6(*b*) and 6(*c*) indicate. Otherwise, the edge effect will have an impact on the response of the directly bonded FBG sensor as well. In addition, when the adhesive length is short, as in the case of Fig. 6(*b*), the maximum displacements of the FBG sensor may vary along its length. In other words, different portion of the FBG may experience different displacement amplitudes. This could lead to the broadening of the FBG spectrum. Therefore, the adhesive length should be sufficiently long to ensure uniform displacement amplitude along the FBG length, as in the case of Fig. 6(*c*).

5.2 Why Does an Adhesive Tape Produce Predominately Forward-Propagating Ultrasound Wave? Wee et al. observed that when cyanoacrylate (CA) was used as adhesive, both forward-propagating and backward-propagating ultrasound waves were generated in the optical fiber [32]. However, when the optical fiber was taped on the structure using an adhesive tape, the forward-propagating waves were much larger in amplitude than the backward propagating waves. When an optical fiber is taped on the structure using an adhesive tape, both direct (i.e., from the structure to the fiber) and indirect (i.e., from the structure to the adhesive tape to the fiber) pathways are active but "the indirect pathway produces the directional coupling" [33]. For the indirect pathway, while the tape is on top of the optical fiber instead of underneath the fiber, the model presented in Fig. 2 still applies, with the adhesive assuming the properties of the tape. Since the exact properties of the CA adhesive or the adhesive tape are not known, a parametric study was carried out to investigate the effect of the adhesive shear modulus—thickness ratio G_a/H_a on the backward/forward ratio, again assuming the excitation signal is a 300 kHz 5.5 cycle tone-burst signal. As shown in Fig. 7(*a*), the backward/forward ratio decreased initially with G_a/H_a. It reaches the lowest value of 0.078 at $G_a/H_a =$ 0.0016 GPa/μm, i.e., the backward propagating wave is almost neglectable as compared with the forward-propagating wave.

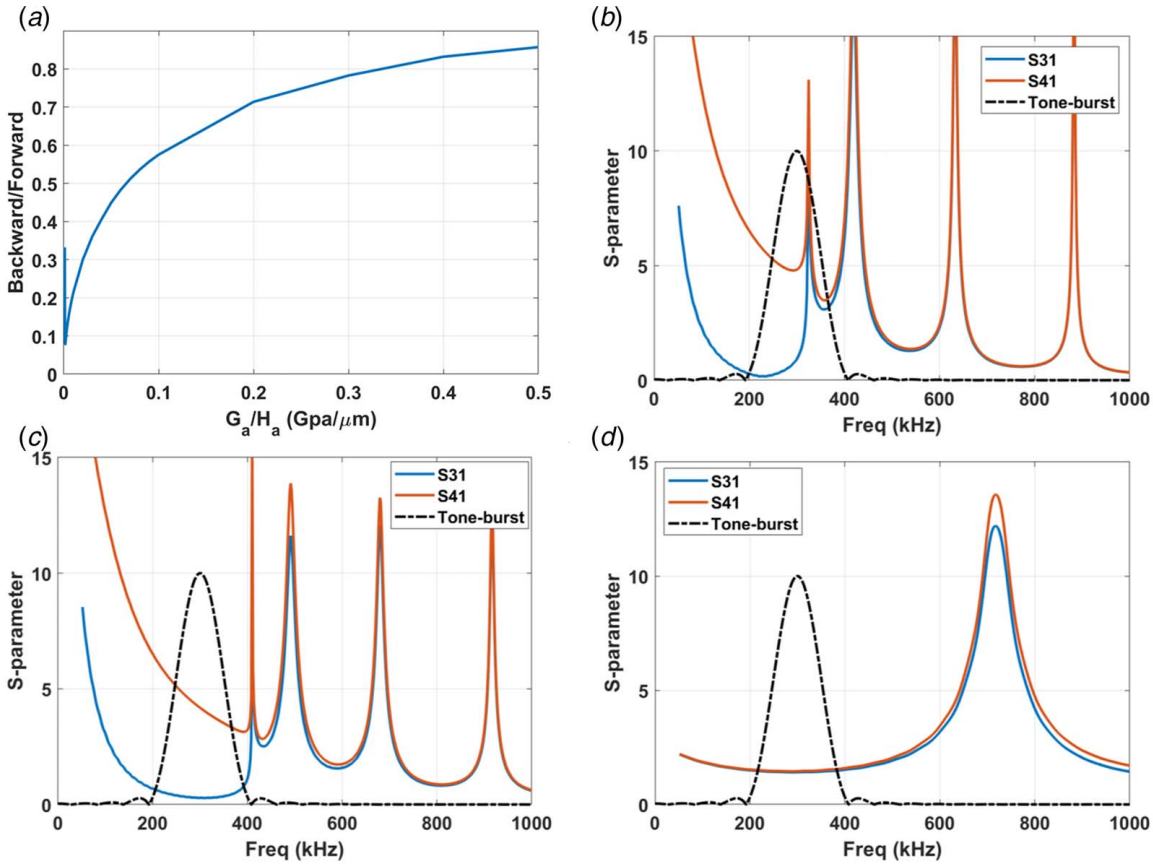

Fig. 7 Effect of the adhesive shear modulus-thickness ratio G_a/H_a on forward and backward coupling: (*a*) backward–forward ratio versus G_a/H_a for a 300 kHz 5.5 cycle tone-burst excitation and comparison of S31 and S41 parameters for G_a/H_a of (*b*) 0.001 GPa/μm, (c) 0.0016 GPa/μm, and (*d*) 0.5 GPa/μm, respectively

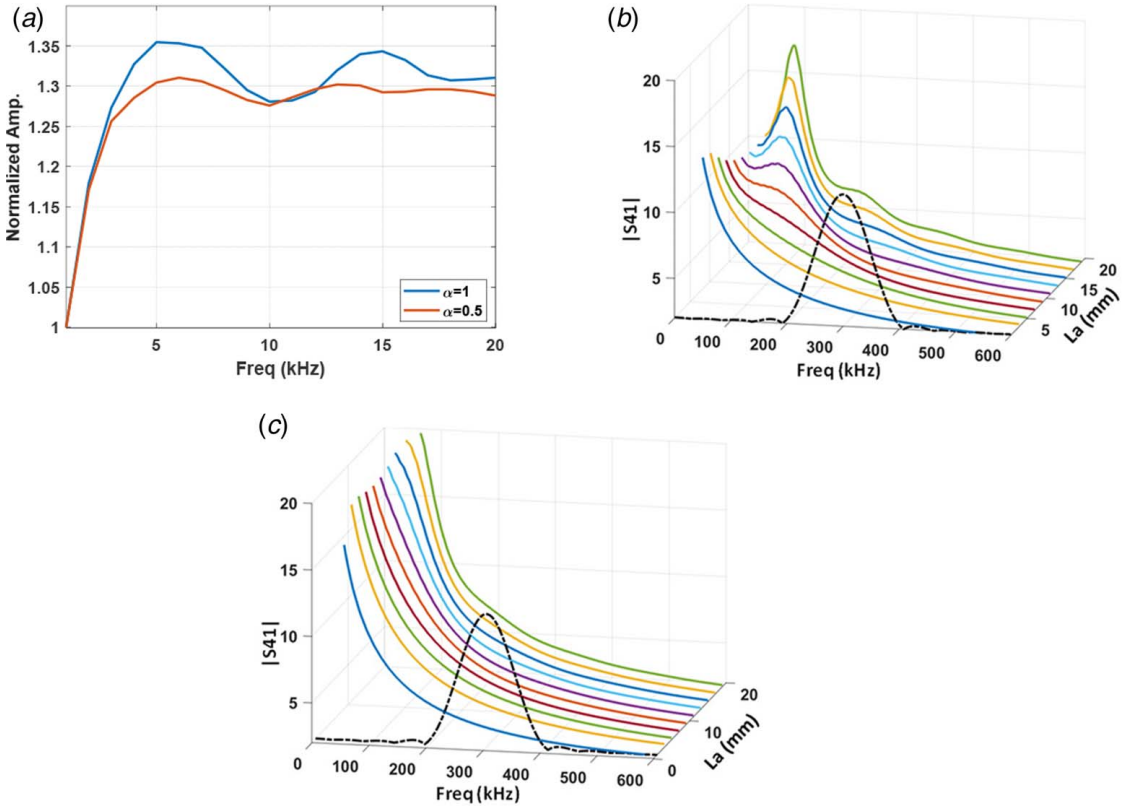

Fig. 8 Effect of the bonding length L_a on (*a*) the maximum displacement at the right edge of the superstrate, assuming a 300 kHz 5.5 cycle tone-burst excitation. The displacements are normalized with respect to the displacement when $L_a = 1$ mm; (*b*) and (c) the S41 parameters at different L_a for a shear transfer ratio of $\alpha = 1$ and 0.5, respectively. The Young's modulus of the adhesive is assumed to be 500 MPa.

Beyond this lowest point, the backward/forward ratio increased steadily with G_a/H_a, reaching 0.8573 for $G_a/H_a = 0.5$. This behavior can be explained by comparing the S31 and S41 parameters, which correspond to the backward- and forward-propagating waves, respectively. Figures 7(*b*)–7(*d*) show these two S-parameters as well as the spectrum of the tone-burst signal for $G_a/H_a = 0.001$, 0.0016, and 0.5 GPa/μm, respectively. The cutoff frequency f_c for $G_a/H_a = 0.001$ and 0.0016 is around 400 kHz, as shown in Figs. 7(*b*) and 7(*c*). For $G_a/H_a = 0.5$ GPa/μm, however, f_c is 7.2 MHz and is out of frequency range shown in Fig. 7(*d*). In this case, the coupler has resonant peaks below the cutoff frequency, such as the one at around 700 kHz in Fig. 7(*d*). Both Figs. 7(*b*) and 7(*c*) show that the two S-parameters have similar amplitudes above f_c. For $G_a/H_a = 0.001$, the cutoff frequency is 409.5 kHz and it falls within the spectrum range of the tone-burst signal. As such, the spectrum components above f_c contribute to the tone-burst response. Since the S31 and S41 parameters above f_c have similar values, the backward/forward ratio is relatively large. Below f_c, however, the S31 and S41 parameters have very different amplitudes with the largest differences being near f_c. In Fig. 7(*c*), f_c is just outside of the tone-burst spectrum range. In this case, the spectral components above f_c no longer contribute to the tone-burst response. Since the tone-burst spectrum covers predominately the frequencies that have the largest differences between the two S-parameters, the backward/forward ratio is the smallest. Notice also that the differences between the two S-parameters decreases at lower frequencies that are further away from f_c. This explains why the backward/forward ratio increases with G_a/H_a since an increasing G_a/H_a leads to a larger f_c and thus increases the spacing between the tone-burst center frequency and f_c. When f_c is very large, e.g., $f_c = 7.2$ MHz for $G_a/H_a = 0.5$, additional resonant peaks appear below f_c and the two S-parameters have similar amplitudes at and near the resonant peak, as shown in Fig. 7(*d*). As a result, the backward- and forward-propagating waves have comparable amplitudes. These results suggest that the backward/forward ratio can be designed by choosing the proper G_a/H_a value.

5.3 Why Does the Coupling Efficiency Increase With the Bonding Length? Wee et al. discovered that the FBG response increases with the adhesive length up to a certain distance [31]. To investigate the effect of the bonding length L_a on the coupling efficiency of the ultrasound coupler, we performed a parametric study on L_a. The maximum displacements at the right edge of the superstrate with different L_a are normalized with the displacement of $L_a = 1$ mm and are plotted in Fig. 8(*a*). Again, the excitation was selected to be a 300 kHz 5.5 cycle tone-burst signal. The Young's modulus of the adhesive was 500 MPa and the thickness was 22 μm [33]. Since the shear transfer ratio of the adhesive is typically unknown, two shear transfer ratios, i.e., $\alpha = 1$ and 0.5, were studied. For $\alpha = 1$, the normalized maximum displacement increased initially with L_a, reaching a maximum value of 1.35 at $L_a = 6$ mm and then decreases with L_a until $L_a = 10$ mm. Its value then fluctuates slightly with L_a. Changing α to 0.5 reduces this fluctuation, making the trend agree better with the experimental results. The S41 parameters for these two cases are shown in Figs. 8(*b*) and 8(*c*). For $\alpha = 1$, the S41 parameters do not have any resonance peak below the cutoff frequency f_c for any bonding length less than 6 mm. A small resonance peak starts to appear when $L_a = 7$ mm. This resonance peak becomes more prominent as L_a increases. In addition, the resonance frequency shifts toward the left and additional resonance peaks, albeit small, appear at higher frequencies as L_a increases. Since the tone-burst frequency was fixed at 300 kHz, the shift of the resonance peaks resulted in the amplitude fluctuation of the tone-burst response. In comparison, the resonance peaks are less prominent, i.e., have lower amplitudes and broader

bandwidths, for $\alpha = 0.5$ and thus the fluctuation of the tone-burst response is less significant. For smaller L_a, however, the amplitude of the tone-burst response is not affected by the shear transfer ratio α. These results suggest that the bonding length L_a should be optimized to achieve the maximum tone-burst response, especially when the shear transfer ratio is large. Unfortunately, the shear transfer ratio of the adhesive is typically unknown. Measuring the shear transfer ratio from the resonance characteristics of the ultrasound coupler could be a subject of future study.

6 Conclusions

The analytical model of an ultrasound coupler, coupling longitudinal waves from one waveguide to the other via the adhesive layer, is developed. We discovered that the ultrasound coupler possesses a cutoff frequency, above which a dispersive longitudinal mode can propagate. Treating the ultrasound coupler as a 4-port network, a semi-analytical model was implemented to calculate its broadband S-parameters. Parametric studies show that the ultrasound coupler displays very different resonant behaviors at frequencies below and above the cutoff frequency and the adhesive properties have strong influences on these behaviors. We also discovered that the unique behaviors of remotely bonded FBG ultrasound sensors are contributed by the resonance of the ultrasound coupler. In the future, more detailed investigations of the resonant characteristics of ultrasound couplers will be carried out using noncontact ultrasound sensing technique with the aim of inversely determining the adhesive properties from the measured resonances. In addition, the source of the resonances and the relationship between the resonance frequency, the wave speed, and the bonding length, will need more detailed investigations.

Acknowledgment

This work is supported by the Office of Naval Research (Grant No. N00014-19-1-2098). The supports and suggestions of the program manager, Dr. Ignacio Perez, are greatly appreciated. Professor Huang also thanks Drs. Wee and Peters at North Carolina State University for stimulating discussions.

Conflict of Interest

There are no conflicts of interest.

Data Availability Statement

The datasets generated and supporting the findings of this article are obtainable from the corresponding author upon reasonable request. Data provided by a third party listed in Acknowledgment.

Appendix

Remotely Bonded Fiber Bragg Grating Ultrasound Sensors. As shown in Fig. 9(*a*), an FBG is a periodic modulation of the refractive index inscribed in the core of a single mode fiber [13]. There are two different ways to interrogate an FBG, i.e., based on the spectrum or the intensity. For spectrum-based interrogation, the FBG is onnected to the broadband source of an optical spectrum analyzer (OSA) through an optical circulator, as shown in Fig. 9(*b*). The broadband light, guided inside the fiber core, is first routed toward the FBG by the circulator. When it encounters the FBG, a portion of the light is reflected at the interfaces with a refractive index change. Since the light reflected at different interfaces have different phases, the superposition of the light results in a reflection with a narrow wavelength λ_B, which is governed by the effective refractive index of the optical fiber n_{eff} and the grating period Λ, i.e., $\lambda_B = 2 n_{eff}\Lambda$. The reflected light is then re-directed by the circulator to the input of the OSA. The OSA outputs the spectrum of the reflected light, based on which the FBG wavelength λ_B can be determined. Ultrasound sensing, however, requires a much higher sampling rate than that of an OSA. To track the high-speed variation of the ultrasound wave, intensity-based interrogation schemes, such as the one shown in Fig. 9(*c*), was developed [59]. The interrogation light, emitted by a laser diode with a narrow wavelength λ_I, is tuned to the midpoint of the slope of the FBG reflection spectrum. The FBG spectrum shifts in response to the ultrasound wave, causing the intensity of the reflected light to fluctuate. This fluctuation can be measured using a photodiode to achieve the required high sampling rate. An FBG ultrasound sensor is typically bonded

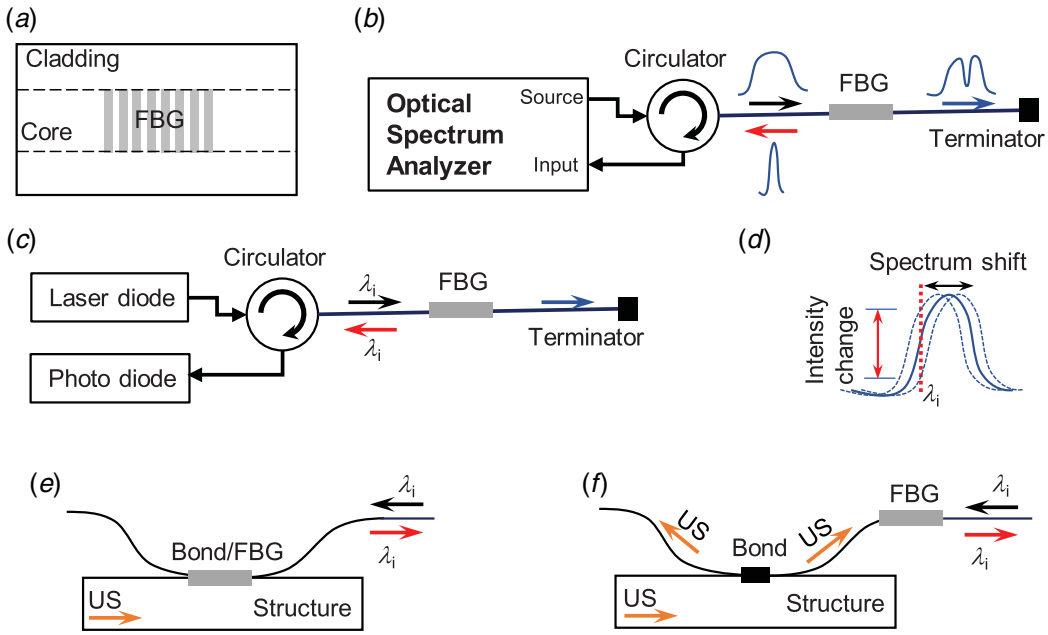

Fig. 9 (*a*) Schematic diagram of a FBG, (*b*) the interrogation of FBG using an optical spectrum analyzer, (*c*) intensity-based interrogation scheme for ultrasound sensing, (*d*) intensity change of the reflected light in response to the FBG spectrum shift due to ultrasound wave, (*e*) directly bonded FBG US sensor, and (*f*) remotely bonded US sensor

directly on a structure using adhesive [60] (see Fig. 9(*e*)). The deformation of the structure is transferred to the FBG via the adhesive layer. As such, the grating period and in turn the FBG reflectance spectrum change with the deformation of the structure. Recently, researchers experimented bonding the optical fiber at a location away from the FBG [28–33]. In these works, the ultrasound wave propagating in the structure is coupled to the optical fiber through the adhesive layer and then propagates along the optical fiber to reach the FBG sensor, as shown in Fig. 9(*d*). As such, the FBG sensor does not measure the deformation of the structure directly. Rather, it measures the displacement of the optical fiber that is coupled from the structure by the adhesive. In other words, "The FBG-inscribed optical fiber was used not only as an optical transmission line but also as an ultrasonic transmission line" [28].

References

[1] Perez, I., DiUlio, M., Maley, S., and Phan, N., 2010, "Structural Health Management in the Navy," Struct. Heal. Monit., **9**(3), pp. 199–207.
[2] Yuan, F. G., 2016, *Structural Health Monitoring (SHM) in Aerospace Structures*, Woodhead Publishing, Cambridge, MA.
[3] Farrar, C. R., and Worden, K., 2007, "An Introduction to Structural Health Monitoring," Philos. Trans. A Math. Phys. Eng. Sci., **365**(1851), pp. 303–315.
[4] Chang, F.-K., 2016, *Structural Health Monitoring 2013, Volume 1 and 2—A Roadmap to Intelligent Structures*, DEStech Publications, Stanford, CA.
[5] Giurgiutiu, V., 2005, "Tuned Lamb Wave Excitation and Detection With Piezoelectric Wafer Active Sensors for Structural Health Monitoring," J. Intell. Mater. Syst. Struct., **16**(4), pp. 291–305.
[6] Raghavan, A., and Cesnik, C. E. S., 2007, "Review of Guided-Wave Structural Health Monitoring," Shock Vib. Dig., **39**(2), pp. 91–114.
[7] López-Higuera, J. M., Cobo, L. R., Incera, A. Q., and Cobo, A., 2011, "Fiber Optic Sensors in Structural Health Monitoring," J. Light. Technol., **29**(4), pp. 587–608.
[8] Chan, T. H. T., Yu, L., Tam, H. Y., Ni, Y. Q., Liu, S. Y., Chung, W. H., and Cheng, L. K., 2006, "Fiber Bragg Grating Sensors for Structural Health Monitoring of Tsing Ma Bridge: Background and Experimental Observation," Eng. Struct., **28**(5), pp. 648–659.
[9] Guo, H., Xiao, G., Mrad, N., and Yao, J., 2011, "Fiber Optic Sensors for Structural Health Monitoring of Air Platforms," Sensors, **11**(4), pp. 3687–3705.
[10] Kahandawa, G. C., Epaarachchi, J., Wang, H., and Lau, K. T., 2012, "Use of FBG Sensors for SHM in Aerospace Structures," Photonic Sens., **2**(3), pp. 203–214.
[11] Majumder, M., Gangopadhyay, T. K., Chakraborty, A. K., Dasgupta, K., and Bhattacharya, D. K., 2008, "Fibre Bragg Gratings in Structural Health Monitoring—Present Status and Applications," Sens. Actuators, A, **147**(1), pp. 150–164.
[12] Todd, M. D., Nichols, J. M., Trickey, S. T., Seaver, M., Nichols, C. J., and Virgin, L. N., 2007, "Bragg Grating-Based Fibre Optic Sensors in Structural Health Monitoring," Philos. Trans. A Math. Phys. Eng. Sci., **365**(1851), pp. 317–343.
[13] Yun-Jiang, R., and Rao, Y. J., 1997, "In-Fibre Bragg Grating Sensors," Meas. Sci. Technol., **8**(4), pp. 355–375.
[14] Jen, C. K., 1985, "Similarities and Differences Between Fiber Acoustics and Fiber Optics," IEEE Ultrasonics Symposium, San Francisco, CA, Oct. 16–18, pp. 1128–1133.
[15] Mbamou, D. N., Helfmann, J., Muller, G., Brunk, G., Stein, T., and Desinger, K., 2001, "A Theoretical Study on the Combined Application of Fibres for Optical and Acoustic Waveguides," Meas. Sci. Technol., **12**(10), pp. 1631–1640.
[16] Shibata, N., Azuma, Y., Horiguchi, T., and Tateda, M., 1988, "Identification of Longitudinal Acoustic Modes Guided in the Core Region of a Single-Mode Optical Fiber by Brillouin Gain Spectra Measurements," Opt. Lett., **13**(7), p. 595.
[17] Safaai-Jazi, A., Jen, C. K., and Farnell, G. W., 1986, "Analysis of Weakly Guiding Fiber Acoustic Waveguide," IEEE Trans. Ultrason. Ferroelectr. Freq. Control, **33**(1), pp. 59–68.
[18] Lee, J. R., and Tsuda, H., 2006, "Sensor Application of Fibre Ultrasonic Waveguide," Meas. Sci. Technol., **17**(4), pp. 645–652.
[19] Lim, S. H., Oh, I. K., and Lee, J. R., 2009, "Ultrasonic Active Fiber Sensor Based on Pulse-Echo Method," J. Intell. Mater. Syst. Struct., **20**(9), pp. 1035–1043.
[20] Fukuma, N., Kubota, K., Nakamura, K., and Ueha, S., 2006, "An Interrogator for Fibre Bragg Grating Sensors Using an Ultrasonically Induced Long-Period Optical Fibre Grating," Meas. Sci. Technol., **17**(5), pp. 1046–1051.
[21] Leal, W. A., Carneiro, M. B. R., Freitas, T. A. M. G., Marcondes, C. B., and Ribeiro, R. M., 2018, "Low-Frequency Detection of Acoustic Signals Using Fiber as an Ultrasonic Guide With a Distant in-Fiber Bragg Grating," Microw. Opt. Technol. Lett., **60**(4), pp. 813–817.
[22] Quero, G., Crescitelli, A., Consales, M., Pisco, M., Cutolo, A., Galdi, V., and Cusano, A., 2012, "Resonant Hydrophones Based on Coated Fiber Bragg Gratings," J. Light. Technol., **30**(15), pp. 2472–2481.
[23] Atkinson, D., and Hayward, G., 2001, "The Generation and Detection of Longitudinal Guided Waves in Thin Fibers Using a Conical Transformer," IEEE Trans. Ultrason. Ferroelectr. Freq. Control, **48**(4), pp. 1046–1053.
[24] Shah, H., Balasubramaniam, K., and Rajagopal, P., 2017, "In-Situ Process- and Online Structural Health-Monitoring of Composites Using Embedded Acoustic Waveguide Sensors," J. Phys. Commun., **1**(5), p. 055004.
[25] Atkinson, D., and Hayward, G., 1998, "Fibre Waveguide Transducers for Lamb Wave NDE," IEE Proc. Sci. Meas. Technol., **145**(5), pp. 260–268.
[26] Neill, I. T., Oppenheim, I. J., and Greve, D. W., 2007, "A Wire-Guided Transducer for Acoustic Emission Sensing," Proc. SPIE 6529, Sensors and Smart Structures Technologies for Civil, Mechanical, and Aerospace Systems, 652913, Apr. 18.
[27] Vogt, T., Lowe, M., and Cawley, P., 2003, "Cure Monitoring Using Ultrasonic Guided Waves in Wires," J. Acoust. Soc. Am., **114**(3), pp. 1303–1313.
[28] Tsuda, H., Sato, E., Nakajima, T., Nakamura, H., Arakawa, T., Shiono, H., Minato, M., Kurabayashi, H., and Sato, A., 2009, "Acoustic Emission Measurement Using a Strain-Insensitive Fiber Bragg Grating Sensor Under Varying Load Conditions," Opt. Lett., **34**(19), p. 2942.
[29] Wee, J., Wells, B., Hackeny, D., Bradford, P., and Peters, K., 2016, "Increasing Signal Amplitude in Fiber Bragg Grating Detection of Lamb Waves Using Remote Bonding," Appl. Opt., **55**(21), pp. 5564–5569.
[30] Davis, C., Norman, P., Rajic, N., and Bernier, M., 2018, "Remote Sensing of Lamb Waves Using Optical Fibres—An Investigation of Modal Composition," J. Light. Technol., **36**(14), pp. 2820–2826.
[31] Wee, J., Hackney, D., Bradford, P., and Peters, K., 2017, "Bi-Directional Ultrasonic Wave Coupling to FBGs in Continuously Bonded Optical Fiber Sensing," Appl. Opt., **56**(25), pp. 7262–7268.
[32] Wee, J., Hackney, D., Bradford, P., and Peters, K., 2018, "Experimental Study on Directionality of Ultrasonic Wave Coupling Using Surface-Bonded Fiber Bragg Grating Sensors," J. Light. Technol., **36**(4), pp. 932–938.
[33] Wee, J., Hackney, D., and Peters, K., 2019, "Preferential Directional Coupling to Ultrasonic Sensor Using Adhesive Tape," Opt. Eng., **58**(7), p. 1.
[34] Wu, Q., Yu, F., Okabe, Y., and Kobayashi, S., 2015, "Application of a Novel Optical Fiber Sensor to Detection of Acoustic Emissions by Various Damages in CFRP Laminates," Smart Mater. Struct., **24**(1), p. 015011.
[35] Yu, F., Okabe, Y., Wu, Q., and Shigeta, N., 2016, "Fiber-Optic Sensor-Based Remote Acoustic Emission Measurement of Composites," Smart Mater. Struct., **25**(10), p. 105033. .
[36] Wee, J., Hackney, D. A., Bradford, P. D., and Peters, K. J., 2017, "Simulating Increased Lamb Wave Detection Sensitivity of Surface Bonded Fiber Bragg Grating," Smart Mater. Struct., **26**(4), p. 1016808.
[37] Islam, M. M. M., and Huang, H., 2014, "Understanding the Effects of Adhesive Layer on the Electromechanical Impedance (EMI) of Bonded Piezoelectric Wafer Transducer," Smart Mater. Struct., **23**(12), p. 125037.
[38] Islam, M. M. M., and Huang, H., 2016, "Effects of Adhesive Thickness on the Lamb Wave Pitch-Catch Signal Using Bonded Peizoelectric Wafer Transducers," Smart Mater. Struct., **25**(8), p. 085014.
[39] Crawley, E. F., De Luis, J., and Luisj, J. D., 1987, "Use of Piezoelectric Actuators as Elements of Intelligent Structures," AIAA J., **25**(10), pp. 1373–1385.
[40] Yan, W., Lim, C. W., Cai, J. B., and Chen, W. Q., 2007, "An Electromechanical Impedance Approach for Quantitative Damage Detection in Timoshenko Beams With Piezoelectric Patches," Smart Mater. Struct., **16**(4), pp. 1390–1400.
[41] Rabinovitch, O., and Vinson, J. R., 2002, "Adhesive Layer Effects in Surface-Mounted Piezoelectric Actuators," J. Intell. Mater. Syst. Struct., **13**(11), pp. 689–704.
[42] M. M. Sadek, 1987, *Industrial Applications of Adhesive Bonding*, Springer, New York, New York.
[43] Ha, S., and Chang, F.-K., 2010, "Adhesive Interface Layer Effects in PZT-Induced Lamb Wave Propagation," Smart Mater. Struct., **19**(2), p. 025006.
[44] Rao, S. S., 2007, *Vibration of Continuous System*, John Willey and Sons, Inc., New Jersey.
[45] Pao, Y.-H., Keh, D.-C., and Howard, S. M., 1999, "Dynamic Response and Wave Propagation in Plane Trusses and Frames," AIAA J., **37**(5), pp. 594–603.
[46] Howard, S. M., and Pao, Y.-H., 1998, "Analysis and Experiments on Stress Waves in Planar Trusses," J. Eng. Mech., **124**(8), pp. 884–891.
[47] Huang, H., and Bednorz, T., 2014, "Introducing S-Parameters for Ultrasound-Based Structural Health Monitoring," IEEE Trans. Ultrason. Ferroelectr. Freq. Control, **61**(11), pp. 1856–1863.
[48] Zahedi, F., and Huang, H., 2017, "Time–Frequency Analysis of Electro-Mechanical Impedance (EMI) Signature for Physics-Based Damage Detections Using Piezoelectric Wafer Active Sensor (PWAS)," Smart Mater. Struct., **26**(5), p. 055010.
[49] Huang, H., 2020, "Resonances of Surface-Bonded Piezoelectric Wafer Active Transducers and Their Effects on the S0 Pitch-Catch Signal," Proc. SPIE11379, Sensors and Smart Structures Technologies for Civil, Mechanical, and Aerospace Systems 2020, 113790I, Apr. 23, p. 18.
[50] Morvan, B., Wilkie-Chancellier, N., Duflo, H., Tinel, A., and Duclos, J., 2003, "Lamb Wave Reflection at the Free Edge of a Plate," J. Acoust. Soc. Am., **113**(3), pp. 1417–1425.
[51] Auld, B. A., and Tsao, E. M., 1977, "A Variational Analysis of Edge Resonance in a Semi-Infinite Plate," IEEE Trans. Sonics Ultrason., **24**(5), pp. 317–326.
[52] Puthillath, P., Galan, J. M., Ren, B., Lissenden, C. J., and Rose, J. L., 2013, "Ultrasonic Guided Wave Propagation Across Waveguide Transitions: Energy Transfer and Mode Conversion," J. Acoust. Soc. Am., **133**(5), pp. 2624–2633.
[53] Schaal, C., and Mal, A., 2016, "Lamb Wave Propagation in a Plate With Step Discontinuities," Wave Motion, **66**, pp. 177–189.
[54] Mallet, L., Lee, B. C., Staszewski, W. J., and Scarpa, F., 2004, "Structural Health Monitoring Using Scanning Laser Vibrometry: II. Lamb Waves for Damage Detection," Smart Mater. Struct., **13**(2), pp. 261–269.
[55] Dewhurst, R. J., Edwards, C., and Palmer, S. B., 1986, "Noncontact Detection of Surface-Breaking Cracks Using a Laser Acoustic Source and an Electromagnetic Acoustic Receiver," Appl. Phys. Lett., **49**(7), pp. 374–376.

[56] Edwards, R. S., Dutton, B., Clough, A. R., and Rosli, M. H., 2011, "Enhancement of Ultrasonic Surface Waves at Wedge Tips and Angled Defects," Appl. Phys. Lett., **99**(9), p. 9.
[57] Ziaja-Sujdak, A., Cheng, L., Radecki, R., and Staszewski, W. J., 2018, "Near-Field Wave Enhancement and 'Quasi-Surface' Longitudinal Waves in a Segmented Thick-Walled Hollow Cylindrical Waveguide," Struct. Heal. Monit., **17**(2), pp. 346–362.
[58] Boonsang, S., 2009, "Photoacoustic Generation Mechanisms and Measurement Systems for Biomedical Applications," Int. J. Appl. Biomed. Eng., **2**(1), pp. 17–23.
[59] Fomitchov, P. A., and Krishnaswamy, S., 2003, "Response of a Fiber Bragg Grating Ultrasonic Sensor," Opt. Eng., **42**(4), pp. 956–963.
[60] Betz, D. C., Thursby, G., Culshaw, B., and Staszewski, W. J., 2006, "Identification of Structural Damage Using Multifunctional Bragg Grating Sensors: I. Theory and Implementation," Smart Mater. Struct., **15**(5), pp. 1305–1312.